Sympathetically cooled highly charged ions in a radio-frequency trap with superconducting magnetic shielding 🅕

Elwin A. Dijck ✉ 🆔 ; Christian Warnecke 🆔 ; Malte Wehrheim 🆔 ; Ruben B. Henninger; Julia Eff; Kostas Georgiou 🆔 ; Andrea Graf; Stepan Kokh 🆔 ; Lakshmi P. Kozhiparambil Sajith 🆔 ; Christopher Mayo 🆔 ; Vera M. Schäfer 🆔 ; Claudia Volk; Piet O. Schmidt 🆔 ; Thomas Pfeifer 🆔 ; José R. Crespo López-Urrutia 🆔

Check for updates

View Online   Export Citation   CrossMark

Articles You May Be Interested In

Underwater sympathetic detonation of pellet explosive

AIP Conference Proceedings (July 2018)

Thermodynamical approach to sympathetic cooling of neutral particles

J. Chem. Phys. (January 2011)

Spectral shape of *in situ* mass spectra of sympathetically cooled molecular ions

Journal of Applied Physics (September 2002)

AIP Publishing

Sympathetically cooled highly charged ions in a radio-frequency trap with superconducting magnetic shielding ⓕ

View Online   Export Citation   CrossMark

Elwin A. Dijck,[1,a] ⓘ Christian Warnecke,[1,2,3] ⓘ Malte Wehrheim,[1,3] ⓘ Ruben B. Henninger,[1]
Julia Eff,[1] Kostas Georgiou,[1,4] ⓘ Andrea Graf,[1] Stepan Kokh,[1] ⓘ Lakshmi P. Kozhiparambil Sajith,[1,5,6] ⓘ
Christopher Mayo,[1,4] ⓘ Vera M. Schäfer,[1] ⓘ Claudia Volk,[1] Piet O. Schmidt,[3,7] ⓘ Thomas Pfeifer,[1] ⓘ
and José R. Crespo López-Urrutia[1] ⓘ

AFFILIATIONS

[1] Max Planck Institute for Nuclear Physics, Saupfercheckweg 1, 69117 Heidelberg, Germany
[2] Heidelberg Graduate School for Physics, Ruprecht Karl University, Im Neuenheimer Feld 226, 69120 Heidelberg, Germany
[3] Physikalisch-Technische Bundesanstalt, Bundesallee 100, 38116 Braunschweig, Germany
[4] School of Physics and Astronomy, University of Birmingham, Edgbaston, Birmingham B15 2TT, United Kingdom
[5] Department of Physics, Humboldt University of Berlin, Newtonstraße 15, 12489 Berlin, Germany
[6] Deutsches Elektronen-Synchrotron DESY, Platanenallee 6, 15738 Zeuthen, Germany
[7] Institute of Quantum Optics, Leibniz University, Welfengarten 1, 30167 Hannover, Germany

[a] Author to whom correspondence should be addressed: elwin.dijck@mpi-hd.mpg.de

ABSTRACT

We sympathetically cool highly charged ions (HCI) in Coulomb crystals of Doppler-cooled Be^+ ions confined in a cryogenic linear Paul trap that is integrated into a fully enclosing radio-frequency resonator manufactured from superconducting niobium. By preparing a single Be^+ cooling ion and a single HCI, quantum logic spectroscopy toward frequency metrology and qubit operations with a great variety of species are enabled. While cooling down the assembly through its transition temperature into the superconducting state, an applied quantization magnetic field becomes persistent, and the trap becomes shielded from subsequent external electromagnetic fluctuations. Using a magnetically sensitive hyperfine transition of Be^+ as a qubit, we measure the fractional decay rate of the stored magnetic field to be at the 10^{-10} s^{-1} level. Ramsey interferometry and spin-echo measurements yield coherence times of >400 ms, demonstrating excellent passive magnetic shielding at frequencies down to DC.

I. INTRODUCTION

Testing fundamental physics in the low-energy, high-precision regime requires sensitive atomic systems in stable and well-characterized environments. Highly charged ions (HCI) feature optical transitions with enhanced sensitivity to potential variation of fundamental constants[1] by virtue of the intrinsically large relativistic effects of their fine-structure transitions,[2,3] crossings of orbital levels,[4–7] and extreme hyperfine effects[8–15] induced by the overlap of the active electron wave function with the nucleus. In addition, systematic frequency shifts caused by AC Stark shifts are strongly suppressed[1] by up to an order of Z^4 within an isoelectronic sequence, where Z is the atomic number. This bears promise for optical atomic clocks reaching relative frequency uncertainties $\Delta\nu/\nu$ at or below the 10^{-20} level.[16] Theory has identified many HCI candidates for testing physics beyond the Standard Model[1] among different isoelectronic sequences, multiplying the number of species having forbidden ground-level transitions within the optical range necessary for an optical clock.

16 October 2023 09:48:25

A general method applied for frequency metrology when a suitable fast-cycling optical transition is not available for state preparation and directly detecting the excitation of the clock transition is quantum logic spectroscopy (QLS).[17] Here, the interrogation of the (highly charged) ion of interest is performed through a co-trapped "logic" ion. A shared motional mode is used for coherently transferring the electronic excitation from the HCI to the logic ion in which it is readily detected. Combined with the sympathetic cooling of HCI[18,19] in a Coulomb crystal, the first coherent laser spectroscopy of any HCI was recently demonstrated.[20] Time dilation frequency shifts were eliminated through algorithmic cooling of weakly coupled motional modes,[21] culminating in a HCI-based optical clock[22] reaching a fractional systematic frequency uncertainty of 2.2×10^{-17}. The application of QLS is rather universal and could be extended to frequency metrology in the extreme ultraviolet (XUV) range.[23] The abundance of highly forbidden, ultra-narrow XUV transitions in HCI and the inception of XUV frequency combs[24–26] have triggered the development of such instruments for HCI frequency metrology.[27,28]

Radio-frequency (RF) ion traps, also known as Paul traps for their Nobel-laureate inventor,[29] enabled the development of quantum optics[30,31] and, more recently, of quantum computing[32–34] and frequency metrology.[35] Characteristics of the trapping environment often set the limits of clock performance.[22] Various electromagnetic perturbations affect the resonance frequency of the reference atomic species for timekeeping. To reduce these and minimize systematic frequency shifts, we developed a novel type of RF ion trap, CryPTEx-SC (Cryogenic Paul Trap Experiment-Superconducting).[36] It comprises a quasi-monolithic superconducting RF resonator with a built-in linear quadrupole trap, which filters the RF drive, shields magnetic field fluctuations, "freezes" the static field present at the onset of superconductivity, and enables coherent operations without the need for external fields and their stabilization.

Here, we present our current CryPTEx-SC setup, including its cryogenic imaging optics (Sec. II), and show selected measurements characterizing the ion trap and verifying the cooling of re-trapped HCI to millikelvin temperature (Sec. III). Finally, we use microwave spectroscopy on Be$^+$ ions to quantify the effectiveness of the superconducting magnetic shielding and the resulting qubit coherence time (Sec. IV).

II. EXPERIMENTAL DESIGN

We produce HCI in a compact electron beam ion trap (EBIT).[37] For laser spectroscopy, the HCI, which are generated with megakelvin temperatures in the EBIT, have to be cooled down to the millikelvin range and below. For this, they have to be re-trapped and sympathetically cooled by a Coulomb crystal of Be$^+$ ions prepared in the cryogenic Paul trap.[18,19]

A. Electron beam ion trap

Within the compact EBIT,[37] permanent magnets generate a magnetic field of 0.86 T at the trap center, which compresses an electron beam of several mA for ionizing injected atoms to high charge states. These ions are then radially confined by the negative space charge of the electron beam. Voltages applied to a set of six drift tubes (see Fig. 1) confine the HCI axially. The highest charge state

is the one with an ionization energy higher than the electron beam energy (up to <6 keV in our device). The ionization time, typically a fraction of a second, is chosen depending on the desired charge state. By pulsing the central drift tube, the HCI inventory is dumped from the trap into the beamline with an initial kinetic energy of about $E_{\text{ion}} \approx 700 \text{ V} \times q$, where q is their electric charge.

B. HCI transfer beamline

A beamline guides the HCI to the Paul trap, comprising several Sikler deflector lenses,[38] an electrostatic bender, and a gradient pulsed drift tube (PDT) for deceleration and compression of the ion bunch, as in CryPTEx-I.[18,19] The pulsed extraction allows for time-of-flight (TOF) selection of the HCI charge state and isotope among the different species produced in the EBIT. Three micro-channel plate (MCP) detectors along the beamline (see Fig. 1) are used for diagnostics. The first one is set behind an aperture in the electrostatic bender in line with the first straight section of the beamline. The other two are mounted on manipulators before and after the spectroscopy trap and can be inserted into the beam path as needed. The second MCP also has a retarding field analyzer (RFA) consisting of two wire-mesh grids mounted in front of it for measuring the HCI bunch kinetic energy. For this, the first grid is grounded, while the second, close to the detector surface, is set to an adjustable positive potential Φ_{grid}, which repels ions with kinetic energy $E_{\text{ion}} < \Phi_{\text{grid}} \times q$ while letting the others pass through. Observing the ion signal while sweeping Φ_{grid} delivers the kinetic-energy distribution of the ion beam.

C. Superconducting resonator Paul trap

CryPTEx-SC combines a quasi-monolithic superconducting RF resonator with a linear Paul trap and is described in detail elsewhere.[36] With a loaded quality factor of $Q \approx 3 \times 10^4$, the niobium RF resonator works as a band-pass filter around the trap drive frequency $\Omega_{\text{RF}} = 2\pi \times 34.3$ MHz. This suppresses RF noise at the sidebands $\Omega_{\text{RF}} \pm \omega_i$ due to the secular frequencies ω_i of ions in the trap, which are induced by the RF drive and lead to motional heating of the ions.[39,40]

Four electrodes produce the quadrupole RF field for radial confinement (see Fig. 1). Each one encloses a co-axial cylindrical inner electrode of the opposite RF phase separated by a narrow 300 μm gap. This increases the capacitance of the resonator and brings its resonance frequency to a value suitable for ion trapping while greatly reducing the required size. Static voltages applied to eight DC electrodes mounted within the quadrupole electrodes confine the ions along the trap axis.

An antenna inserted into the niobium resonator[36] sends microwaves for driving the Be$^+$ ^{2}S$_{1/2}$ $(F = 1) \leftrightarrow (F = 2)$ transition at 1.25 GHz (see Fig. 12). It is made of niobium wire with a length of 57 mm, forming a $\lambda/4$ antenna mounted at a $\approx 20°$ angle to the horizontal plane in order to couple to all polarization modes. Its efficiency is affected by higher-order resonances in the resonator trap; the return loss over the operational frequency range is a few dB. Microwaves are fed from a function generator (Sinara Urukul) referenced to a GPS-disciplined quartz oscillator (TimeTech RefGen) and amplified by a 50 dB amplifier (Mini-Circuits HPA-25W-272+).
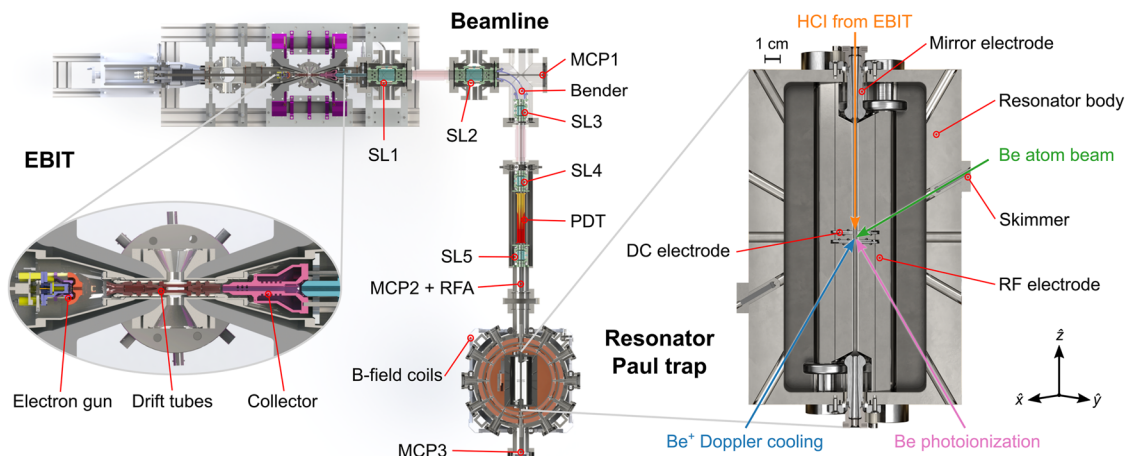
FIG. 1. Top-down overview of the experiment. An electron beam ion trap (EBIT) generates HCI by electron-impact ionization. The ions are transferred to the CryPTEx-SC Paul trap through a beamline equipped with five Sikler lenses (SLs), an electrostatic bender, and a pulsed drift tube (PDT) for ion deceleration and bunching. Three micro-channel plate (MCP) detectors are used for diagnostics; the second one is equipped with a retarding field analyzer (RFA) for kinetic energy determination. After injection into the Paul trap, HCI are confined by mirror electrodes at both ends of the four RF blade electrodes. Eight DC electrodes shape the central axial potential, where HCI are sympathetically cooled by Be^+ ions. We define a coordinate system aligned with the principal trap axes as indicated; $\hat{x}$ and $\hat{y}$ are rotated 45° out of the image plane.

Magnetic fields for trap quantization are applied by three orthogonal pairs of coils approximating a Helmholtz configuration and can reach up to about 200 μT.

A frequency-quadrupled solid state laser system (Toptica TA FHG pro) delivers several mW of 235 nm light to produce Be^+ ions inside the trap by resonant two-step photoionization. The Be atoms come from a resistively heated oven mounted about 93 cm away from the trap center. It emits an atomic beam collimated by several apertures before reaching the trap region through an 800 μm diameter skimmer (see Fig. 1), preventing Be contamination of the superconducting surfaces.

D. Doppler-cooling laser

A second frequency-quadrupled UV laser system (Toptica TA FHG pro) is used for Doppler cooling on the Be^+ $1s^2\,^2S_{1/2}-1s^2\,^2P_{3/2}$ transition at 313 nm. An acousto-optic modulator (AOM) stabilizes its power and allows fast switching of the light. When the quantization axis defined by the magnetic field is well aligned with the laser propagation axis and the laser is circularly polarized, a closed transition between the states $^2S_{1/2}$ ($F = 2$, $m_F = \pm 2$) – $^2P_{3/2}$ ($F = 3$, $m_F = \pm 3$) can be driven. In general, some repumping from the $F = 1$ upper ground state (see Fig. 12) is necessary. To this end, we split off some 313 nm laser light and shift its frequency by 1.25 GHz with a combination of AOMs. Both laser beams are stably pointed to the trap by piezo-driven mirrors (MRC Systems) controlled by a pair of position-sensitive detectors. The beams are overlapped, circularly polarized, and enter the trapping region at an angle of 30° to the trap axis (see Fig. 1). The handedness of polarization is set by a $\lambda/4$ waveplate mounted in a motorized rotation stage.

E. Cryogenic imaging optics

Non-destructive detection of ions inside a Paul trap is usually accomplished by imaging with lens systems[41–46] in combination with cameras and photomultiplier tubes (PMTs). For cryogenic environments, single, bi-aspheric lenses[47] and reflecting Schwarzschild objectives[48] have been developed. These systems are usually separated only a few millimeters from the ions to ease manufacturing requirements and reduce their size. Here, we have designed an optical system (see Fig. 2) to accommodate the relatively long distance to the trapped ions of about 60 mm. The fluorescence emitted by the Be^+ ions at 313 nm is refocused by an NA = 0.36 eight-lens objective. For this wavelength, we use UV fused silica (UVFS) and calcium fluoride (CaF_2) lenses with a maximum diameter of 50.8 mm, most of them stock models (see Table I).

To avoid a reduction of the quality factor of the resonator trap by dielectric materials inside it, the 4 K objective is mounted on its top with a superconducting chevron grid with 90% transmission for light but blocking RF. The resulting working distance is 57 mm. The whole stack can be adjusted radially by 1 mm to compensate for misalignments. Each optical element is centered by a partially segmented ring with 40 contact blades manufactured from anodized aluminum (0.25 mm thick) to absorb differential thermal contraction of the Al, CaF_2, and UVFS materials during the cool-down. In the axial direction, spacer rings made from anodized aluminum in direct contact with the lenses set their separation and guarantee guided alignment. Their thicknesses are adjusted to measured lens dimensions to compensate for manufacturing tolerances. A non-anodized aluminum cylindrical cage holds rings, spacers and lenses, and shields anodized parts from thermal radiation. Apertures in its surface ensure efficient pumping between the lenses. A 3 mm longitudinal cut reduces radial compression of the inner elements during cool-down.

On the air side, a detection unit consisting of two PMTs and a camera is mounted on top of the vacuum chamber (see Fig. 3). The EMCCD [electron-multiplying charge-coupled device (CCD)] camera (Andor iXon Ultra 888) has a pixel pitch of 13 μm and is capable of resolving the ion positions in the trap.
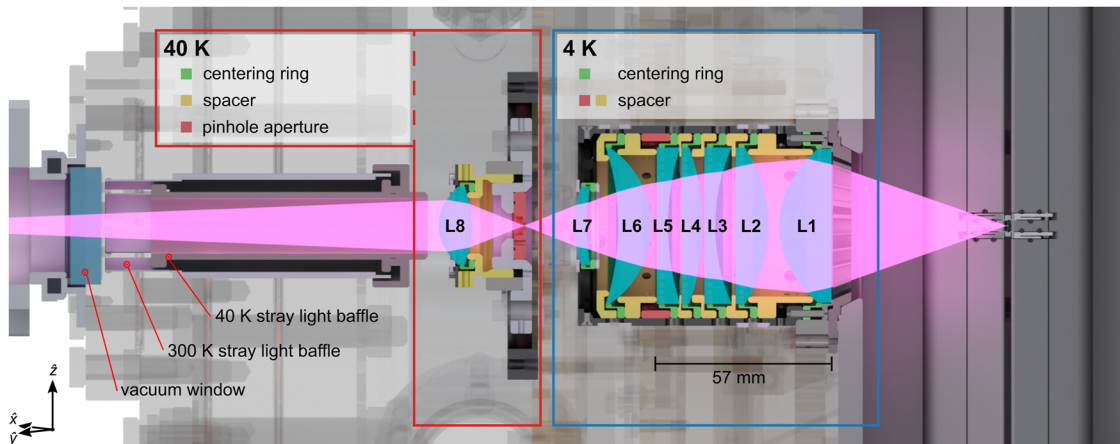
FIG. 2. Vertical cross section through the cryogenic objective (left is up toward the detection setup). Starting from the trap side, lenses L1–L7 are held by centering rings (green) and separated by spacers (yellow, red), projecting an intermediate image of the laser-cooled Be^+ ions through a 2 mm pinhole (red, 40 K stage) at 157 mm from the trap center. This aperture reduces the heating of the 4 K stage by room-temperature black-body radiation. A custom bi-aspheric lens, L8, is mounted on the 40 K stage for relaying the intermediate image to the EMCCD camera focal plane and PMTs for fluorescence detection. The holder for L8 (light gray) is radially positioned by four set screws, and the focal distance is adjustable by a thread (yellow). Its 5 mm axial travel allows a magnification on the final image in a range of 8× to 20×. Stray light from the lasers is blocked by two coaxial, thermally decoupled cylindrical shields attached to the 40 K stage and vacuum window flange, respectively.

TABLE I. Table of lenses. The last column indicates the axial distance from the preceding element at the lens center. Magnification is set by the distance to lens L8; the quoted distance yields about 10×.

Lens	Vendor	Product id	Distance (mm)
L1	Edmund Optics	67 268	57.0
L2	Newport	SPX043	3.5
L3	Knight Optical	67 112	6.6
L4	Lambda Research	PCX-50.8u-150	0.5
L5	EKSMA Optics	112–5519E	4.3
L6	Thorlabs	LE4412	1.8
L7	Thorlabs	LE5414	10.3
L8	Asphericon	150 111-000-03C	33.0

Rubber bellows and a linear stage are used to bring it into focus.

A 50/50 beam splitter moving along with the camera sends 313 nm light to the first PMT. Its housing contains a beam block for protection against overexposure as well as a spatial filter located in the focal plane of L8 for rejecting background light. It consists of two knife edges in the vertical direction and two in the horizontal direction that can be moved independently using fine threads. A second PMT setup (e.g., to detect light from Be^+ photoionization or for HCI spectroscopy) sits directly on top of the vacuum chamber and includes a lens for refocusing light of other wavelengths.

Simulations performed with the software OSLO (Optics Software for Layout and Optimization) indicate a spatial resolution of the lens stack of about 110 line pairs per mm at the 20% point of the modulation transfer function. This is compatible with the in-air characterization with a resolution test target illuminated by 313 nm light through a diffusive element mounted close to the target, which demonstrates a 10%–90% intensity rise distance of

$d_{10-90\%} = 6.9(0.3)$ μm in object space (see Fig. 4). This is sufficient to resolve two trapped Be^+ ions at an axial secular frequency of up to approximately $\omega_{z,0} \approx 2\pi \times 1.5$ MHz. Even at the lowest magnification of 8×, this corresponds to a separation of several pixels on the camera. Depending on the material properties, the performance of the lens system deviates with temperature from that of the carefully aligned setup at 300 K.[49]

III. ION-TRAP CHARACTERIZATION

To characterize the strength of the axial and radial trapping fields, the secular frequencies of trapped Be^+ ions were measured by exciting the respective motional degrees of freedom. This was achieved by applying an oscillating "tickling" electric field to the mirror electrode behind the trap. Secular motion driven at resonance causes elongation of the ion images on the camera and a drop in fluorescence rate (see Fig. 5). One of the methods of calibrating the magnification factor of the imaging system was using the ion separation distance on the camera image of an axial two-ion Be^+ crystal at a known axial secular frequency.

Micromotion caused by stray electric fields is minimized by a combination of observing the ion position along the $(\hat{x} - \hat{y})/\sqrt{2}$ axis on the camera image as a function of radial trapping potential[50] and using the RF-photon correlation technique[51,52] to reduce displacement along the $(\hat{x} + \hat{y})/\sqrt{2}$ axis (orthogonal to the image plane). In the latter method, modulation of the Be^+ fluorescence rate in sync with the RF trapping field cycle is investigated. We obtain the timestamp of PMT counts with nanosecond resolution from a Sinara DIO module. Because this module and the function generator driving the trap are phase-locked to a common clock signal, finding the time relative to the RF phase is a simple modulo operation with the known trap drive frequency Ω_{RF}. Figure 6 shows a typical RF-photon correlation measurement, where the residual oscillating electric field
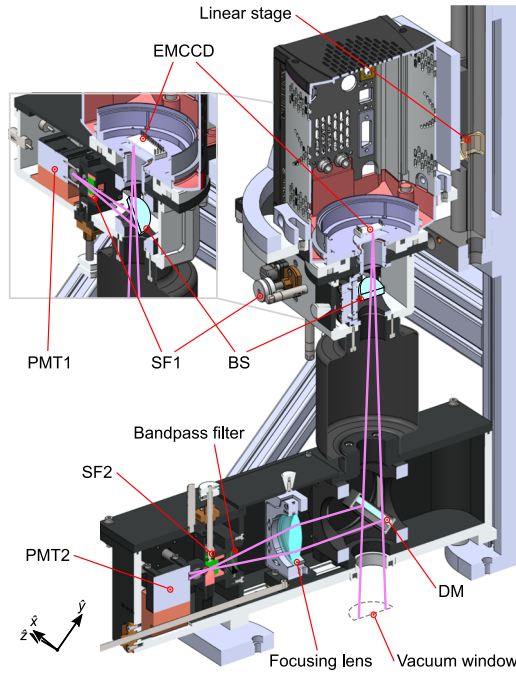
FIG. 3. Air-side imaging and fluorescence-detection setup mounted on top of the vacuum chamber. EMCCD: electron-multiplying charge-coupled device; PMT1: photomultiplier tube for cooling-ion fluorescence detection; PMT2: same, for spectroscopy ion fluorescence; SF1, SF2: adjustable spatial filters; DM: dichroic mirror; BS: 50/50 beam splitter.
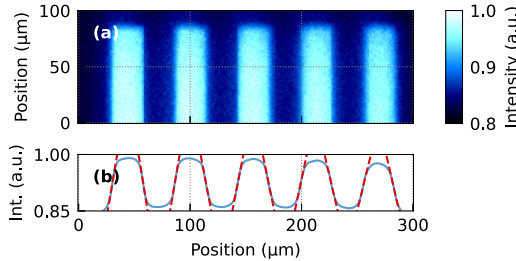

FIG. 4. Knife-edge spatial resolution test of the lens system at $10.4\times$ magnification at room temperature. (a) Cut-out from an in-air EMCCD image of an NBS 1963A resolution-test target with 18 line pairs per mm illuminated by 313 nm light. (b) Projection across the lines; the mean 10%–90% intensity rise distance is $d_{10-90\%} = 6.9(0.3)$ μm.

component[52] at the ion position was minimized to $|\hat{k} \cdot \vec{E}_{\mathrm{RF}}| \leq 16$ V/m.

A. Retrapping highly charged ions

We now turn to the procedure for preparing cold highly charged ions in the spectroscopy trap. Usual breeding times for argon ions of charge states 10^+ to 16^+ in the EBIT are on the order of hundreds of milliseconds for a 10 mA electron beam with an energy of about 1 kV. By switching the potential of the central drift tube with a high-voltage switch, the trap is inverted, and ions are emitted
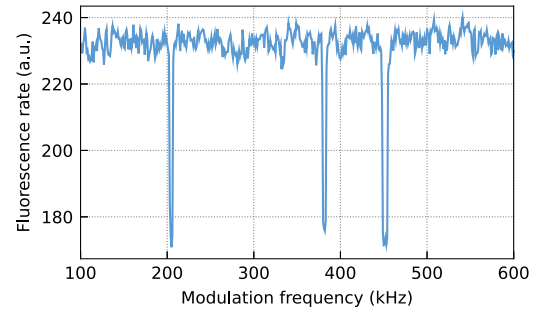

FIG. 5. Example of a secular frequency determination. Fluorescence rate as a function of tickling frequency. Three clear resonances are visible, corresponding to the axial and two radial center-of-mass secular frequencies.
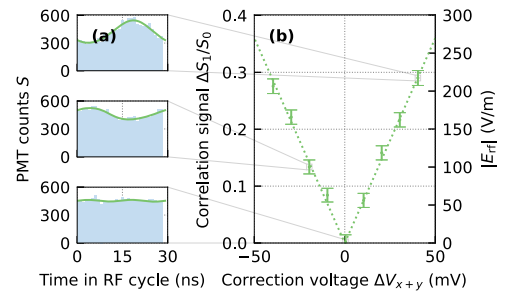

FIG. 6. Minimization of micromotion using RF-photon correlation. (a) The observed modulation ΔS_1 at the trap RF frequency Ω_{RF} of the average fluorescence rate S_0 is minimized by (b) moving the ion along the $(\hat{x} + \hat{y})/\sqrt{2}$ axis. Note that here the direction of induced micromotion has a component along the cooling laser propagation direction $\hat{k}$ as it is orthogonal to the displacement. The right-hand scale indicates the corresponding oscillating electric field amplitude E_{RF} at the (displaced) mean ion position.

into the beamline. Based on results from identical miniature EBITs, a single dump contains several million ions in various charge states. They can be separated using time-of-flight (TOF) spectroscopy, and undesired species are filtered out by pulsing a kicker electrode. The initial kinetic energy is reduced in a pulsed drift tube (PDT) before reaching the spectroscopy trap, which can be positively biased to control the final kinetic energy.

After setting the EBIT parameters for producing the desired HCI, we iteratively optimize the voltages applied to the beamline electrodes for maximum transmission, select the species by TOF, and minimize the kinetic energy spread of the ion bunches.

In general, the EBIT produces ions with a distribution of charge states depending on the continuous or pulsed influx of neutral atoms and the ratio of the rates for electron-impact ionization and photorecombination. Isotopes and residual gas impurity ions also appear in the TOF spectra. Each ion bunch separates according to the extant charge-to-mass ratios [see Fig. 7(a)]. For an ion of charge q and mass m,

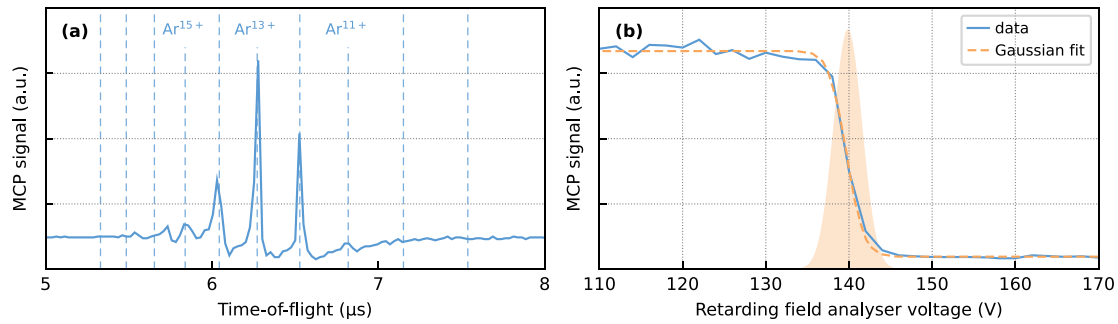$$t \propto \frac{1}{\sqrt{q/m}} . \tag{1}$$

FIG. 7. Characterization of the HCI transfer beamline. (a) Example of Ar HCI time-of-flight (TOF) at an EBIT extracting rate of 0.7 Hz; peaks correspond to different charge states present due to the constant injection of neutral Ar into the EBIT. Vertical dashed lines show a fit with Eq. (1) for argon, marking the peaks as labeled. The charge-breeding time can be used to optimize the yield of the desired charge state. (b) Normalized kinetic energy distribution for $^{40}Ar^{14+}$ after optimizing the bunching in the pulsed drift tube. The Gaussian fit yields an energy spread (1σ) of about 1.7 V × q.

For selecting a HCI species of interest, one electrode of SL3 is pulsed to let only ions within a time window of a fraction of a μs pass, while at other times deflecting unwanted ions.

After beamline optimization, the ions are bunched and decelerated with a pulsed drift tube.[19] It reduces the mean kinetic energy of the ions as well as their energy spread. Its timing is very critical, and in most cases, only a single charge state is decelerated. Downstream, a second MCP is used to measure and optimize the kinetic energy distribution [see Fig. 7(b)] with its attached retarding-field analyzer by sweeping the retarding potential Φ_{grid}. At the end of the beamline, the HCI are brought from the initial mean kinetic energy of 700 V × q down to about 140 V × q, low enough for the following retrapping step but keeping the ion beam from diverging too much before reaching the spectroscopy trap.

After passing through two Einzel lenses mounted on the heat shields, the HCI enter the superconducting linear Paul trap. The entire trap is biased to a positive potential set about 1 V below the HCI kinetic energy to further slow them down on entering the trap. A cylindrical mirror electrode is mounted at each end of the about 15 cm long quadrupole trap (see Fig. 1). After briefly pulsing down the one facing the beamline to allow HCI to enter, both mirror electrodes stay at a higher potential reflecting the HCI back and forth under radial RF confinement. The closing timing is carefully optimized to prevent HCI from leaving the trap after the first reflection.

At this point, the residual kinetic energy of the HCI is still larger than the axial trap depth in the section in the middle of the quadrupole electrodes. Following the established technique,[18,19] an ion crystal consisting of several dozen laser-cooled Be$^+$ ions is prepared beforehand. On each pass through the crystal, while oscillating between the mirror electrodes, the HCI dissipate energy, transferring it to the laser-cooled ion crystal through the Coulomb interaction. They eventually reach a standstill after some hundreds of reflections, forming a mixed-species crystal with the Be$^+$ ions. Then, sympathetic cooling by the Be$^+$ ions ensures reaching mK temperatures.

Since HCI do not interact with the Doppler-cooling laser, their signature on the crystal images is a dark spot with a radius larger than the distance between individual Be$^+$ ions due to the

stronger Coulomb repulsion. Examples of mixed crystals containing one argon or one xenon HCI are displayed in Fig. 8. Charge exchange reactions with residual gas molecules, primarily hydrogen in the cryogenic trap, reduce the lifetime of the HCI to about 5–10 min. We plan to reduce the vacuum conductance in the inner trap region by closing off ports with windows wherever possible and lowering the operating temperature of the trap to increase its lifetime.

B. Charge-state determination

For verifying the charge state of a re-trapped HCI, we examine the enclosing ion crystal. The HCI is strongly coupled to the Be$^+$ ions, and its effect depends on its charge-to-mass ratio. Two sensitive ion crystal properties are its structure and secular mode frequencies. To calculate their dependence on the co-trapped HCI species, we consider the potential energy of an ion crystal in the harmonic pseudopotentials of the trap and the Coulomb repulsion. For a crystal of N ions with charges q_i and masses m_i at positions $\vec{r}_i = (x_i, y_i, z_i)$, the
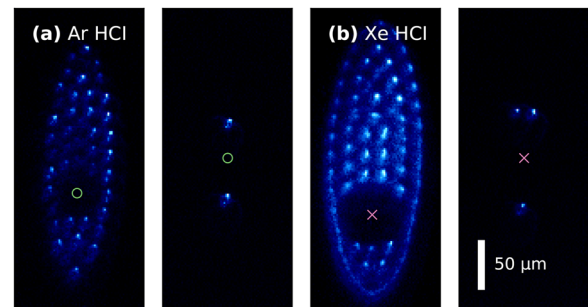

FIG. 8. Examples of mixed-species crystals consisting of Be$^+$ ions and (a) one argon or (b) one xenon HCI. The left-hand image displays a larger crystal immediately after (re-)capturing one HCI. Such crystals are exposed to the excitation of Be$^+$ secular motion while suspending Doppler cooling to reduce the number of Be$^+$ as needed.

potential energy is given by[53]

$$V(\vec{r}_1, \ldots, \vec{r}_N) = \sum_i \frac{1}{2} m_i \left(\omega_{x,i}^2 x_i^2 + \omega_{y,i}^2 y_i^2 + \omega_{z,i}^2 z_i^2 \right)$$
$$+ \frac{1}{4\pi\varepsilon_0} \sum_{i \neq j} \frac{q_i q_j}{|\vec{r}_i - \vec{r}_j|} . \quad (2)$$

Here, the trap depth is parameterized by the secular frequencies $\omega_{k,i}$, which depend on the charge and mass of the ion i. Defining the secular frequencies for a single Be^+ ion with $q_0 = +1e$ and $m_0 = 9.01$ u as nominal frequencies $\omega_{k,0}$, the secular frequencies for a HCI of charge $q_i = \theta_i q_0$ and mass $m_i = \mu_i m_0$ are related to the nominal frequencies as

$$\omega_{x,i}^2 = \frac{\theta_i}{\mu_i} \frac{\omega_{x,0}^2 - \omega_{y,0}^2 - \omega_{z,0}^2}{2} + \frac{\theta_i^2}{\mu_i^2} \frac{\omega_{x,0}^2 + \omega_{y,0}^2 + \omega_{z,0}^2}{2},$$
$$\omega_{y,i}^2 = \frac{\theta_i}{\mu_i} \frac{\omega_{y,0}^2 - \omega_{x,0}^2 - \omega_{z,0}^2}{2} + \frac{\theta_i^2}{\mu_i^2} \frac{\omega_{x,0}^2 + \omega_{y,0}^2 + \omega_{z,0}^2}{2}, \quad (3)$$
$$\omega_{z,i}^2 = \frac{\theta_i}{\mu_i} \omega_{z,0}^2 .$$

The equilibrium positions $\vec{r}_{eq,i}$ of an ion crystal for given confinement strengths $\omega_{k,0}$ can be found by minimizing Eq. (2).

As an example, we calculate the equilibrium positions for the type of ion crystal needed for quantum logic, consisting of one Be^+ ion and one HCI. Assuming sufficiently strong radial confinement $\omega_{z,0} \ll \omega_{x,0}, \omega_{y,0}$, the crystal will be oriented along the trap axis with $x_{eq,i} = y_{eq,i} = 0$. The equilibrium positions of the two ions are the solution to

$$\left. \frac{\partial V}{\partial z_i} \right|_{z_i = z_{eq,i}} = 0 . \quad (4)$$

This can be solved analytically to yield

$$z_{eq,Be^+} = \mp \frac{\theta_{HCI}}{(1 + \theta_{HCI})^{2/3}} \ell_0 , \quad z_{eq,HCI} = \pm \frac{1}{(1 + \theta_{HCI})^{2/3}} \ell_0 , \quad (5)$$

where ℓ_0 is the characteristic length scale, defined as

$$\ell_0 = \sqrt[3]{\frac{q_0^2}{4\pi\varepsilon_0 m_0 \omega_{z,0}^2}} . \quad (6)$$

Note that the positions only depend on the charge state of the HCI and not on its mass. For larger ion ensembles, numerical minimization may be used in Eq. (4). A small modification of this configuration may be caused by light forces acting on the Doppler-cooled Be^+ ions but not on the HCI, which is neglected in Eq. (2).

To determine the charge state of re-trapped HCI, we analyze the ion positions in axial linear mixed crystals. An example with one Ar HCI and three Be^+ ions is depicted in Fig. 9. Observed and calculated equilibrium positions are compared by minimizing Eq. (2) values for different assumed charge states, q_{HCI}. We thus conclude that the dark spot in Fig. 9 contains a $^{40}Ar^{10+}$ ion. Note that in this ion configuration, it is in fact possible to obtain the charge state of the HCI independent of the secular frequency from the position of the inner Be^+ ion relative to the outer Be^+ ions.
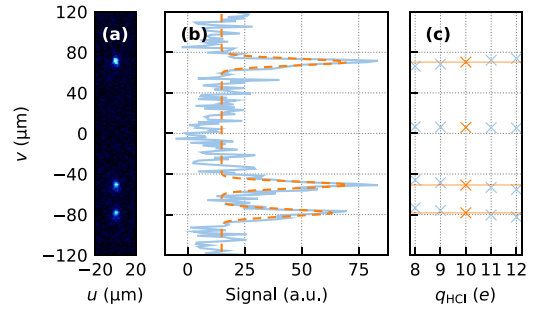

FIG. 9. Example charge-state determination for an axial linear crystal consisting of a ^{40}Ar HCI co-trapped with three $^9Be^+$ ions. (a) Crystal image showing Be^+ fluorescence. (b) Ion positions as fitted with three two-dimensional Gaussian functions and a constant background to the image (dashed line). (c) Comparison of calculated (crosses) at $\omega_{z,0} = 2\pi \times 118.3$ kHz to fitted equilibrium positions (horizontal lines, uncertainty smaller than line thickness). The position of the inner Be^+ ion indicates a HCI charge state of $q_{HCI} = +9.8(0.2)e$.

C. Spatial thermometry

After establishing the HCI charge state, recorded images of mixed crystals can be used to determine ion temperatures. Ions in thermal equilibrium randomly move in the trapping potential, and their spatial probability distribution is visible on camera images. For a single Be^+ ion at temperature T in a harmonic potential in the weak-binding limit, the time-averaged spatial distribution in each of the three principal trap directions k (averaged over time) is Gaussian with an approximate width of[54,55]

$$\sigma_{th,k,0} = \sqrt{\frac{k_B T}{m_0 \omega_{k,0}^2}} . \quad (7)$$

Here, we neglect micromotion, which would slightly increase the width in both radial directions[56] but remains below the level of a few percent for small values of the Matthieu stability parameter $q \ll 1$.

In a mixed-species ion crystal, all motional modes are thermally excited following the kinetic energy distribution. The width of the spatial distribution in direction k for ion i is then given by[55]

$$\sigma_{th,k,i} = \sqrt{\sum_p S_{k,i,p} \frac{k_B T}{m_i \omega_{k,p}^2}} = \sqrt{\gamma_{k,i}^2 \frac{k_B T}{m_0 \omega_{z,0}^2}} , \quad (8)$$

where the sum runs over all normal modes p of the crystal, with mode frequencies $\omega_{k,p}$ and eigenvectors $S_{k,i,p}$. In general, at a given temperature T, the spatial extent for each ion is different; by normalizing all values to the one of a given Be^+ ion from Eq. (7), the scaling for each ion can be expressed in a set of weighting factors $\gamma_{k,i}$ that depend only on the crystal configuration and the ratios of the radial secular frequencies to the axial secular frequencies. Note that for a crystal consisting purely of Be^+ ions, $\omega_{z,0}$ is the frequency of the axial center-of-mass mode.

We obtain the motional modes of a crystal by numerically solving the eigensystem describing secular ion motion as a perturbation of its equilibrium position, defining $\vec{r}_i(t) = \vec{r}_{eq,i} + \vec{\Delta r}_i(t)$. When an ion is cold enough, the local potential around it can be approximated as being harmonic by linearizing all forces. The Lagrangian for the

axial secular motion is written in terms of the displacements Δz_i and corresponding velocities $\Delta \dot{z}_i$ as

$$L_z = \frac{1}{2}\sum_i m_i \Delta \dot{z}_i^2 - \frac{1}{2}\sum_{i,j} \left.\frac{\partial^2 V}{\partial z_i \partial z_j}\right|_{\Delta z_i=0} \Delta z_i \Delta z_j, \qquad (9)$$

taking the potential V from Eq. (2) and equilibrium positions from Eq. (4). The axial eigenmodes ($\omega_{z,p}$, $S_{z,i,p}$) of the crystal are then numerically obtained from the corresponding equations of motion, and the calculation is repeated for the two radial directions.

The spatial extent of ion i on the camera image is the convolution of its projected spatial probability distribution and the point-spread function (PSF) of the imaging system. Assuming an approximately Gaussian PSF, this convolution results in

$$\sigma_{u,i} = \sqrt{\sigma_{\text{PSF},u}^2 + \sigma_{\text{th},u,i}^2} \quad \text{and} \quad \sigma_{v,i} = \sqrt{\sigma_{\text{PSF},v}^2 + \sigma_{\text{th},v,i}^2}, \qquad (10)$$

denoting the two image axes as u, v. In our experimental setup, one image axis corresponds to the axial coordinate of the trap, while the other axis mixes both radial coordinates under a 45° angle (see Sec. II C). We obtain the projected spatial extents by way of Eq. (8), defining the effective weighting factors as

$$\gamma_{u,i} = \sqrt{\frac{\gamma_{x,i}^2 + \gamma_{y,i}^2}{2}} \quad \text{and} \quad \gamma_{v,i} = \gamma_{z,i}. \qquad (11)$$

For the trapping parameters of the crystal in Fig. 9, the calculated weighting factors $\gamma_{u,i}$ and $\gamma_{v,i}$ are given in Table II. Note that normalizing to the nominal axial secular frequency in Eq. (8) means that the $\gamma_{v,i}$ values in this table are independent of the axial secular frequency, whereas the $\gamma_{u,i}$ values depend on the ratios of the two radial secular frequencies to the axial secular frequency. The observed horizontal and vertical spatial extents of the ions in the crystal of Fig. 9 obtained from the two-dimensional Gaussian fits to the image data are shown in Fig. 10. From Eq. (10), it is clear that a thermal contribution would show as a relative difference in spatial extent between the ions that follows the pattern of the weighting factors in Table II.

The results of a global fit to the observed spatial extents are shown as colored bars in Fig. 10, taking $\sigma_{\text{PSF},u}$, $\sigma_{\text{PSF},v}$ and T as free parameters. The fitted temperature of the Be$^+$ ions is $T = 4(3)$ mK. We can assume thermal equilibrium due to the strong ion-ion Coulomb interaction, and thus this temperature also holds for the Ar^{10+} ion, confirming the cooling of HCI to millikelvin temperatures close to the Doppler limit. The uncertainties from spatial
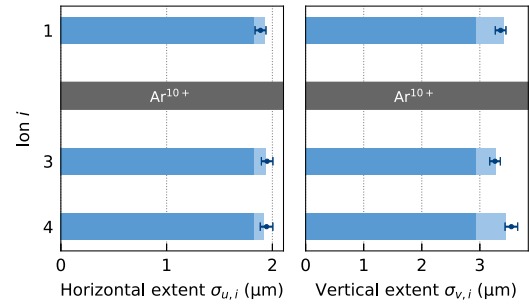

FIG. 10. Spatial thermometry of mixed-species crystal in Fig. 9. The data points with error bars represent the spatial extent of Be$^+$ ions on the image in the horizontal (u) and vertical (v) coordinates, corresponding to radial and axial trap coordinates, respectively. Bars show a fit with Eq. (10). The (small) difference in ion spatial extent following the relative factors given in Table II is the signature of a thermal component; the fit yields a temperature of $T = 4(3)$ mK. The darker part of the bars shows the PSF contribution, taken to be identical for all ions.

thermometry are relatively large, mostly because it requires resolving a small thermal component blurred by the larger PSF contribution. Assuming a symmetric Gaussian PSF, the relation $\sigma_{\text{PSF}} = d_{10-90\%}/(2\sqrt{2}\,\text{erf}^{-1}\,0.8)$ holds, which indicates general agreement between these PSF values and the in-air characterization of the cryogenic optics described in Sec. II E.

The method of preparing cold HCI is also applicable to other species, as illustrated by Fig. 8. The dynamics of the mixed-species ion crystals are primarily determined by the charge-to-mass ratio of the HCI vs that of the cooling ion. In general, a mismatch in this parameter results in weak coupling between the HCI and cooling ion in some motional modes, decreasing sympathetic cooling efficiency. As the lightest singly charged ion favorable for laser cooling, Be$^+$ is the most versatile cooling species for a great variety of HCI charges and masses, although in some cases, Mg$^+$ or Ca$^+$ may also be suitable. Moreover, the recently developed algorithmic cooling in Paul traps[21] solves the problem of cooling weakly coupled modes. This makes switching between HCI species in the experiment relatively easy, and generally, an optimization of EBIT, ion optics, and the timing of the deceleration pulses is all that is needed.

IV. SUPERCONDUCTING MAGNETIC SHIELDING

A unique feature of CryPTEx-SC is its ability to permanently freeze a pre-set magnetic field flux. When a hollow superconductor is cooled below its critical temperature T_c in a finite magnetic field, the onset of perfect diamagnetism expels an extant external field from the bulk material by inducing eddy currents on its outer and inner surfaces. This freezes the magnetic flux inside the hollow, as already observed by Meissner and Ochsenfeld.[57]

Niobium, a type-II superconductor, exhibits flux pinning when the expulsion of magnetic flux from the bulk of the superconductor is not complete, forming flux tubes at pinning centers such as lattice imperfections or impurities. This effect is stronger in thin layers. Trapped flux causes finite surface resistance in superconducting radio-frequency (RF) cavities.[58]

We observe some influence of the magnetic field strength at the time of cooling down below $T_c = 9.2$ K on the quality factor of the

TABLE II. Numerically calculated spatial thermometry weighting factors for an axial linear crystal consisting of a single Ar^{10+} ion co-trapped with 3 Be$^+$ ions. Horizontal axis (u) corresponds to the radial trap coordinate; the vertical axis (v) corresponds to the axial trap coordinate (see main text for details).

	Ion	Image horizontal $\gamma_{u,i}$	Image vertical $\gamma_{v,i}$
1	Be$^+$	0.291	0.665
2	Ar^{10+}	0.123	0.358
3	Be$^+$	0.319	0.536
4	Be$^+$	0.304	0.640

resonator. When operating it in a superconducting state at higher RF input powers, a reduction depending on the value of the magnetic field trapped during the last cool-down is seen (see Fig. 11). For this measurement, we repeatedly warmed up the resonator above T_c using a resistive heater, applied an external magnetic field, and let the resonator cool down to $T = 4.2$ K again. The maximum applied magnetic field magnitude of 0.6 mT is far below the critical field strength H_c of order 100 mT for niobium; therefore, the material always reached the Meissner state.

Reflective measurements of the unloaded quality factor Q_0 of the quadrupole resonance at 35 MHz were performed with a network analyzer at 20 dBm input power connected to the inductive coupler. An increase of 0.5 mT in $\vec{B}$-field magnitude reduces Q_0 by about 5% with an associated 10^{-7} fractional shift of the resonance frequency. The highest quality factor is reached at a finite vertical magnetic flux density compensating for the background $\vec{B}$-field component. Note that the magnetic field from the field coils might not be homogeneous throughout all of the resonator material.

The resonator quality factor Q_0 can be written in terms of the geometry factor G and the surface resistance R_s at the relevant RF frequency ω_0 as[59]

$$Q_0 = \frac{G}{R_s}. \tag{12}$$

The geometry factor is the ratio of the magnetic field strength integrated over the cavity volume to that integrated over the cavity surface,[59]

$$G = \frac{\omega_0 \mu_0 \int_V |\vec{H}|^2 \, dv}{\int_S |\vec{H}|^2 \, ds}, \tag{13}$$

which only depends on the resonator geometry. For our cavity, we calculate it with the finite-element method (FEM) to be $G = 1.7\ \Omega$. If we assign the observed change in Q_0 to an increase in the surface resistance related to flux trapping, our data appear to suggest a nonlinear dependence rather than the typical linear dependence at low $\vec{B}$-field strength.[60] Figure 11 shows an empirical least-squares fit assuming a power-law behavior for $R_s \propto |\vec{B}|^n$, yielding $n \approx 0.3$. However, we note that we only observe this $\vec{B}$-field dependent effect
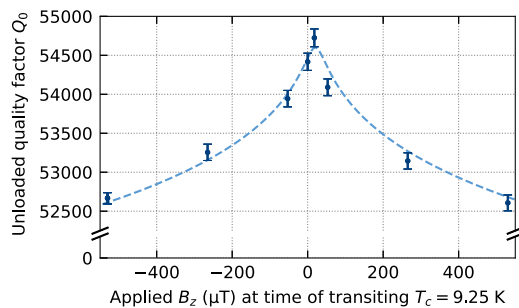

FIG. 11. Unloaded quality factor Q_0 of the 35 MHz quadrupole resonance at $T = 4.2$ K for high input power as a function of the vertical magnetic flux density applied at the time the superconductor was cooled below T_c. The dashed line is an empirical fit assuming a power law for the surface resistance $R_s \propto |\vec{B}|^n$ yielding $n \approx 0.3$. Maximum Q_0 is reached at a finite positive B_z that cancels the background magnetic field.

at high in-coupled power. At low power, Q_0 is higher, reaching $Q_0 \approx 200\,000$, and shows no dependence on $|\vec{B}|$ over the studied range. A similar interplay with the intra-cavity electric field magnitude has been associated with hydride-formation in Nb superconducting cavities,[61] suggesting that this process may also play a role in the overall performance of our cavity. In any case, under current operating conditions, the effect of the trapped flux used as the quantization axis for the ions does not significantly limit trap performance.

A. Microwave hfs spectroscopy

Generally, magnetic-field insensitive hyperfine transitions are chosen as qubits for quantum information processing to limit decoherence caused by fluctuating external fields. By operating at a specific ("magic") magnetic field magnitude, one ground state hyperfine transition component in Be$^+$ can be made first-order insensitive to magnetic field fluctuations at a finite field magnitude.[62] However, here we investigate magnetically sensitive hyperfine-structure (hfs) transitions in order to benchmark the superconducting shielding performance of our trap.

The magnetic field in the trap was characterized by microwave spectroscopy on single Be$^+$ ions (see Fig. 12) using the transition $|\downarrow\rangle = |F = 2, m_F = -2\rangle$ to $|\uparrow\rangle = |1, -1\rangle$ with an on-resonance Rabi time of 33 μs. We apply the Ramsey method with time-separated oscillatory fields to obtain good frequency resolution.[63] Pulse sequences are implemented using the ARTIQ (Advanced Real-Time Infrastructure for Quantum physics) experiment control system[64] to run the RF signal generators for the AOMs, the microwave source, and for recording the signal from the PMT.

The sequence starts with both the cooling and repumper 313 nm lasers switched on for Doppler cooling (see Fig. 13). State preparation consists of turning off the repumper laser so that the cooling laser, which is not entirely free of a π-polarized component, pumps the Be$^+$ ion with the highest probability into the upper qubit state $|\uparrow\rangle$. Subsequently, the cooling laser is also turned off, and a microwave pulse sequence comprised of a $\pi/2$ pulse, a variable wait time T_R and a second $\pi/2$ pulse is executed. For state detection, the cooling laser is unblocked, and fluorescence is recorded for a set time matching the timescale of optical pumping. If the sequence leaves the ion in the $|\uparrow\rangle$ state, no fluorescence appears; if, instead, the microwave radiation successfully flips the qubit to the lower state $|\downarrow\rangle$, fluorescence will be observed until the ion is pumped into the dark qubit state $|\uparrow\rangle$ again. This timescale, which depends on the purity of
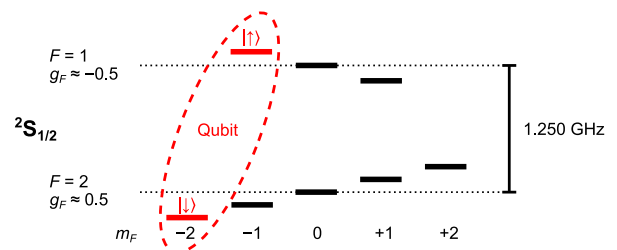

FIG. 12. Hyperfine structure of the $^2S_{1/2}$ ground state of ^{9}Be$^+$. The transition component $(F, m_F) = (2, -2) \leftrightarrow (1, -1)$ with maximal first-order Zeeman shift is chosen as the qubit for most of this work.
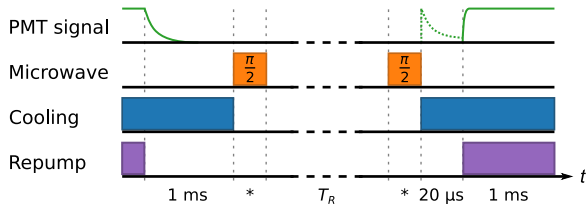
FIG. 13. Ramsey-pulse sequence: switching scheme of microwave radiation, cooling, and repumper laser. Sketched is also the fluorescence signal measured with the PMT. See the main text for details.
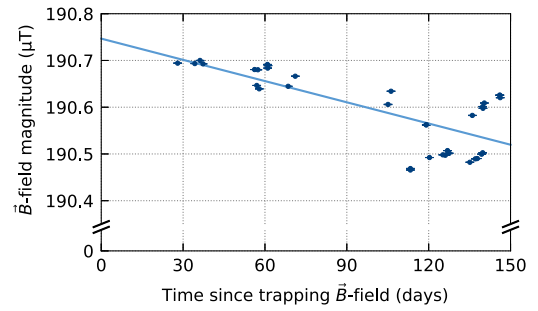

FIG. 15. Long-term stability of the magnetic flux trapped inside the superconducting resonator, with its magnitude decreasing less than 0.2% over several months. The fitted exponential decay would yield an effective lifetime of about 300 years. Uncertainties are smaller than the symbols; variation in the chosen trapping parameters causes scatter in the data.

the circular polarization of the laser, its intensity, and the alignment between its propagation direction and the quantization axis, limits the signal-to-noise ratio for a single detection trial. After the detection time window, both lasers are unblocked for 1 ms to (re-)cool the ion, and then the sequence can be repeated.

As a function of the frequency detuning, the observed transition probability shows the characteristic Ramsey pattern (see Fig. 14), where the width of its envelope depends on the Rabi time and the fringe spacing on $1/T_R$. While accurate resonance frequency determination requires long wait times, finding the central one among the many fringes becomes cumbersome. For this, we combine a series of frequency scans with different frequency ranges and values of T_R. We identify the central peak at each T_R directly[65] using a global least-squares fit of the Ramsey pattern[63] yielding the transition frequency.

B. Decay of trapped magnetic flux

Using the method described earlier, the frequency of the magnetic field sensitive transition was measured, yielding the Zeeman splitting and the $\vec{B}$-field magnitude at the ion position. After trapping a magnetic flux in the superconductor of about 190 μT at the

trap center, the external field coils were switched off, and measurements were performed over several months (see Fig. 15), during which the resonator was kept below its critical temperature.

From the measured frequency of the qubit hfs transition, we subtract the zero-field hyperfine splitting, known to 10^{-11} precision,[66] and obtain the Zeeman shift $\Delta\nu_Z$. In the first order, the magnetic field magnitude is then

$$|\vec{B}| = \frac{h\Delta\nu_Z}{\mu_B\Delta(g_F m_F)},\quad (14)$$

where the numerical factor for the qubit transition is given by $\Delta(g_F m_F) \approx 1.5018$, corresponding to a magnetic field sensitivity of 21 kHz/μT. To include quadratic and higher order coupling between the ground state hyperfine levels, we use the Breit–Rabi formula.[66] Figure 15 shows how the trapped magnetic field magnitude decreased by only about 0.1% over 100 days. Assuming a continuous
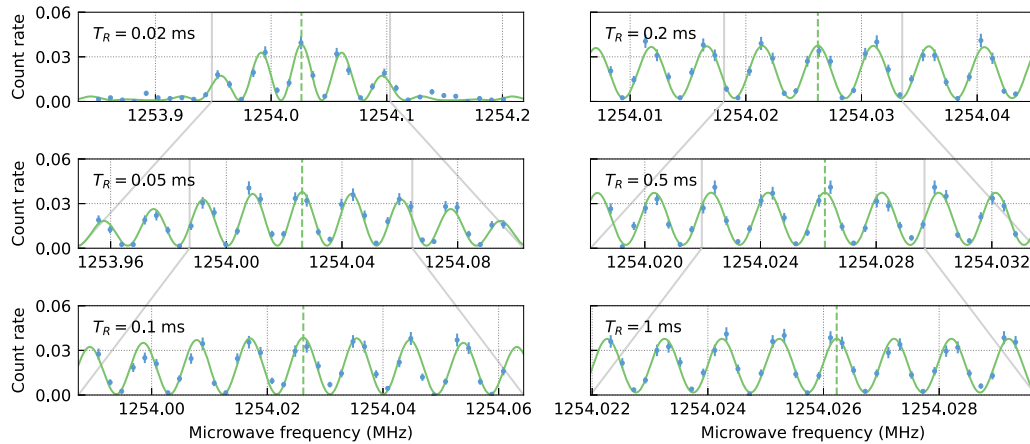

FIG. 14. Example Ramsey measurement series showing the observed fluorescence rate vs the microwave frequency near the qubit hfs transition. The data are for wait times T_R between 20 μs and 1 ms, adapting the frequency range and step size at each T_R to keep the number of measured fringes roughly constant. The line shows a global fit of the excitation probability; a dashed vertical line marks the fitted resonance frequency. Each data point is averaged over 2000 sequences, and uncertainties are derived from Poisson statistics. The $\vec{B}$-field magnitude at the ion position determined from this series is 190.5026(3) μT. At this time, the magnetic field was not well-aligned with the cooling laser propagation direction, resulting in few signal photons per repeat due to rapid optical pumping into dark states.

exponential decay, the least-squares-fitted lifetime of the trapped $\vec{B}$-field is about 300 years, which would correspond to a continuous fractional change in the magnitude of

$$\frac{1}{|\vec{B}|}\frac{d|\vec{B}|}{dt} \approx 1 \times 10^{-10} \text{ s}^{-1}. \tag{15}$$

During longer measurement series, we observe frequency drifts consistent with $\vec{B}$-field changes at this order of magnitude. However, these drifts are non-monotonic and, at least in part, appear to correlate with temperature fluctuations in the cryogenic system. Small changes of ion position in a $\vec{B}$-field gradient could also cause frequency shifts, which we explore further in Sec. IV E. The scatter in the right half of Fig. 15 corresponds to a greater variation in trap operating parameters chosen during this period.

Presently, we cannot establish whether the $\vec{B}$-field decay is continuous (aside from flux quantization) or possibly activated by operation at high RF input power or superconductor temperature. The lifetime may thus represent an effective value for typical trap operation. In any case, the long-term stability of the pre-set quantization $\vec{B}$-field demonstrated here is a great advantage for quantum experiments, comparable to operation with permanent magnets.[67] There, thermal drifts determine the long term field stability; we similarly find that stabilizing the resonator temperature by a proportional-integral-differential (PID) loop controlling current through a heating resistor mounted on the resonator body yields the most stable conditions for qubit operation.

C. Shielding of external magnetic fields

Fluctuating external magnetic fields can induce decoherence. We now investigate how efficiently the superconducting resonator shields the trapped ions from environmental magnetic noise. Our outermost shielding within the vacuum chamber consists of nested OFHC (oxygen-free high conductivity) copper heat shields[36] that are nearly identical to those of the sister experiment[20,47] at Physikalisch-Technische Bundesanstalt (PTB), Braunschweig. These shields filter magnetic field noise above corner frequencies of 0.14–0.30 Hz along different axes by inducing counteracting eddy currents, as characterized in the PTB trap.[47]

Moreover, our superconducting resonator also shields magnetic field changes down to zero frequency. We determine the effective DC shielding factor by observing the qubit resonance frequency while applying external fields using each pair of coils in turn. Figure 16 shows the results for a variable DC external field along the trap axis, which is at a 30° angle to the direction of the previously trapped $\vec{B}$-field. A linear component as a function of the externally applied field is apparent here. We calculate the shielding factor for the trapped ion as the ratio of the observed change to the expected change without the superconductor by a linear least-squares fit, resulting in 761(18), with the uncertainty reflecting the spread in the data. The fact that the shielding is not complete could be caused by the various openings in the resonator housing, where magnetic field lines may be able to slowly penetrate the inner volume. Changes in qubit frequency using the other two pairs of coils are consistent with the same shielding factor, taking into account the relative angles of the applied fields. This demonstrates a passive magnetic shielding of about 57 dB at frequencies down to DC, comparable to some dedicated magnetically shielded rooms[68] employing
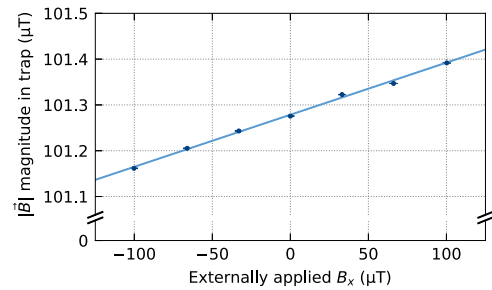

FIG. 16. DC magnetic shielding: $\vec{B}$-field flux density at the ion position from qubit resonance frequency vs externally applied $\vec{B}$-field (under a 30° angle). Note the different axis scales. Uncertainties are smaller than the symbol size.

nested shields of μ-metal. We can assume that for higher frequencies, the total shielding factor of our setup is at least as good as the product of this and the component from the OFHC heat shields.[47]

D. Qubit coherence time

Magnetic noise, as well as power and frequency fluctuations of the microwave source driving the Be^+ qubit, reduce its coherence time. The microwave function generator is referenced to a clock signal with a stability of $10^{-10}\sqrt{s}/\sqrt{\tau}$ over time τ. We investigate the qubit decoherence by two methods: observing the Ramsey fringe contrast, which is sensitive to low-frequency noise[69] (T_2^*), and spin-echo sequences sensitive to high-frequency noise (T_2).

Decoherence manifests in a contrast reduction of the Ramsey pattern with increasing wait time T_R. A series with wait times T_R of up to 500 ms is shown in Fig. 17. We determine the contrast by varying the detuning of the microwave pulses. The functional shape of the decoherence as a function of wait time depends on the noise spectrum. If Gaussian phase noise is the dominant process, the coherence depends on the relative length of the noise correlation time τ and the experimental cycle.[70] For T_R shorter than the noise correlation time, the coherence exhibits a Gaussian decay $\propto e^{-t^2/(2\tau^2)}$, which at longer wait times turns into an exponential decay $\propto e^{-t/T}$. The contrast in Fig. 17 shows Gaussian reduction pointing to a noise-correlation time on the order of the maximum wait time. A least-squares fit yields $\tau = 414(22)$ ms.
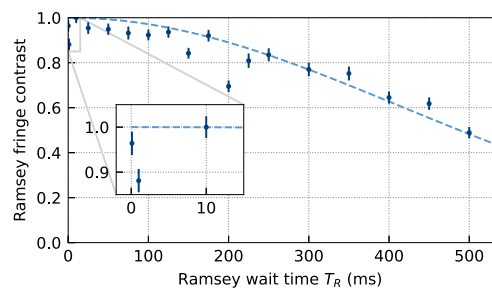

FIG. 17. Measurement of Ramsey fringe contrast as a function of wait time T_R up to 500 ms. The reduction in contrast is consistent with non-Markovian noise; a Gaussian fit (dashed line) indicates a $1/\sqrt{e}$ coherence time of $\tau = 414(22)$ ms.

In the Hahn spin-echo sequence,[71] a π-pulse is added at the midpoint of the wait time in a Ramsey sequence (see inset Fig. 18). This reverses the low-frequency phase evolution of the spin, refocusing in the second half a phase rotation accrued in the first half. This cancels the effect of slow drifts of the qubit frequency, leaving dephasing by random noise dominant. Contrary to the Ramsey case, the refocusing pulse causes the qubit to end up in the same state it started in when driven on resonance. Decoherence will increase the probability of ending in the other state, with both probabilities becoming equal when coherence is completely lost. To independently measure signal and background, we interleave sequences where the final pulse affects a $3\pi/2$ spin rotation, thereby inverting the probabilities of reaching either state.

Results of spin-echo measurements where T_{wait} was varied between 100 μs and 4 s are shown in Fig. 18. The probability of finding the correct state decreases with T_{wait}, becoming close to random at the longest wait time. A least-squares Gaussian fit yields $\tau = 2200(100)$ ms. This coherence time is significantly longer than in the Ramsey case and shows the refocusing effect of the spin-echo method. Assuming the decoherence to be caused by Gaussian $\vec{B}$-field noise, its root-mean-square fluctuations can be quantified as[47,70]

$$\sqrt{\langle \Delta B \rangle^2} \approx \frac{\hbar}{\mu_B \Delta(g_F m_F)} \frac{1}{\tau}, \qquad (16)$$

which gives a root-mean-square (rms) noise amplitude of 3.5(0.2) pT.

E. Single qubit addressing

These long coherence times allow us to greatly reduce the intensity of the microwave radiation while still coherently exciting the qubits, thus increasing the Rabi time and reducing the frequency width of the excitation. By measuring the qubit resonance frequency of a single ion moved along the trap axis near its center, we observed in the trapped $\vec{B}$-field an undesired gradient of 0.1 μT/mm. While this can be eliminated with the external field coils in the next cool-down, its presence allows us to distinguish two simultaneously trapped Be$^+$ ions based on the difference in resonance frequencies. Figure 19 shows that by increasing the Rabi time to 150 ms, we are able to independently excite two Be$^+$ qubits separated by about
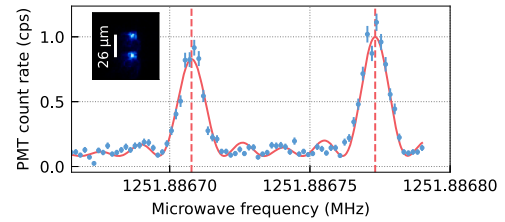

FIG. 19. Individual addressing of two Be$^+$ simultaneously trapped qubits. A small $\vec{B}$-field gradient splits the two transition frequencies apart by 60 Hz, resolvable when attenuating the microwave intensity by about 70 dB. The fit comprises two Rabi line shapes whose widths are consistent with the Rabi time of 150 ms. Inset displays an EMCCD image of the two-ion axial crystal.

60 Hz. The small difference in peak height is explained by a position-dependent light collection efficiency; we see the same effect when moving a single ion along the trap axis.

Magnetic field gradients in combination with ion motion are also a potential source of decoherence. The ion motion is described by a thermal distribution of quantized harmonic oscillations, treated in more detail in Sec. III C. Using Eq. (7) with a typical axial secular frequency of $\omega_{z,0} \approx 2\pi \times 215$ kHz and an ion temperature of $T \approx 0.5$ mK close to the Be$^+$ Doppler temperature,[72] we find an rms length scale of $\sigma_z \approx 0.5$ μm. In the $\vec{B}$-field gradient, this corresponds to an rms $\vec{B}$-field magnitude of about $\sigma_B \approx 50$ pT. However, during the Ramsey and spin-echo measurements, the cooling lasers are blocked, and no thermalization takes place, which results in purely harmonic ion motion without heating. Such motion would lead to an effect that is periodic in the wait time at the oscillation period and not the observed decoherence.

V. DISCUSSION

We have demonstrated the primary feature of our CryPTEx-SC experiment: preparing cold highly charged ions in a low-noise trap for precision spectroscopy. The HCI are produced in an electron beam ion trap before re-trapping and sympathetic cooling in a crystal of ^{9}Be$^+$ ions pre-loaded in the cryogenic radio-frequency trap for spectroscopy. The trap features a multi-lens cryogenic objective with a large numerical aperture and working distance designed to minimize black-body radiation in the trap region. Analysis of mixed ion crystal images enabled identification of the HCI charge state and confirmation of reaching mK temperatures.

The setup is similar to its sister experiment[22] at PTB, Braunschweig, but has the unique feature of integrating the linear RF ion trap with a superconducting resonator,[36] which minimizes magnetic field noise without requiring active field stabilization. This is beneficial for coherent manipulations of ion qubits, including quantum logic spectroscopy techniques. Flux trapping in the superconducting niobium preserves the $\vec{B}$-field present at the time of cool-down, making stable external quantization fields unnecessary and eliminating associated technical noise. By performing microwave spectroscopy on the ground state hyperfine structure of Be$^+$ ions, we found the fractional decay of the stored $\vec{B}$-field to be on the order of 10^{-10} s^{-1}. The presence of a small $\vec{B}$-field gradient along the trap axis optionally enables individual qubit addressing.
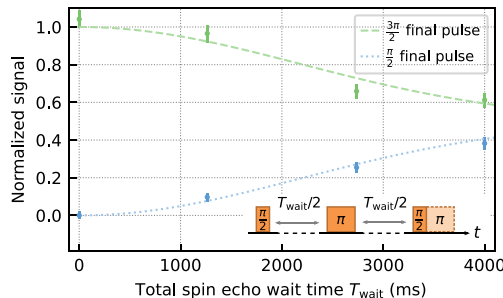

FIG. 18. Spin-echo measurement with a total wait time of up to 4 s. Inset shows the pulse sequence, where the final pulse controls whether the $|\uparrow\rangle$ or $|\downarrow\rangle$ state is reached in the absence of decoherence. A Gaussian fit (dashed line) yields a $1/\sqrt{e}$ coherence time of $\tau = 2200(100)$ ms.

Moreover, the superconductor passively attenuates external magnetic field fluctuations down to zero frequency with a measured shielding factor at DC of 57 dB. At finite frequencies (above about 0.1 Hz), the two copper thermal shields enclosing the spectroscopy trap provide additional shielding.[47] Using Ramsey measurements, we observe coherence times of >400 ms on the maximally $\vec{B}$-field sensitive Be$^+$ qubit without active field stabilization or AC line triggering, over an order of magnitude longer than reported for the PTB trap without superconducting shielding[47] and comparable to experiments implementing permanent magnets and double μ-metal shielding.[67] In spin-echo measurements, where slow drifts are canceled, the observed coherence time of 2.2(0.1) s corresponds to Gaussian $\vec{B}$-field noise with a root-mean-square amplitude of $\sqrt{\langle \Delta B \rangle^2} = 3.5(0.2)$ pT. Potential remaining sources of decoherence include external $\vec{B}$-field noise intruding through the openings in the resonator, noise on the DC trap electrodes, ion motion in the $\vec{B}$-field gradient, ion heating, and microwave noise. Quantum lock-in techniques could be implemented[73] to further investigate the noise spectrum.

Longer coherence times in trapped ion qubits have been demonstrated for transitions intrinsically insensitive to $\vec{B}$-field fluctuations[74] using decoherence-free subspaces[75] or dynamic decoupling.[76] The latter techniques add overhead to experimental procedures and increase demands on gate fidelity. Our results show that in a cryogenic ion trap that is passively shielded by the combination of enclosing superconducting material and copper thermal shields, reaching long coherence times is not limited to magnetically insensitive trapped ion qubits. This is advantageous for direct extreme-ultraviolet frequency-comb spectroscopy,[28] optical clocks,[22,35] as well as quantum computing[77] and simulation[78] with trapped ions.

Currently, we are setting up a laser system for driving Raman transitions in Be$^+$ for sideband cooling and quantum logic spectroscopy of HCI. Planned improvements in the vacuum system and the RF coupling will lead to lower operating pressure and longer lifetimes of the trapped HCI. The present setup is the blueprint for an upgraded superconducting trap (project VAUQSI), which will soon be assembled.

Advancing the trapping and cooling of HCI will bring opportunities for fundamental physics research with this large class of atomic systems. Our superconducting-resonator trap-design uses passive shielding to provide an ultra-stable electromagnetic environment for quantum logic spectroscopy. Although phonon heating rates have yet to be measured, we expect that the strong filtering of RF noise by the resonator will also prove favorable in this regard. Long coherence times enable the excitation of narrow transitions with long Rabi times. The demonstrated low $\vec{B}$-field noise could be beneficial not only for HCI research but also for other atomic and molecular ions. In particular, the decoherence rate in our trap will be a great advantage for future quantum logic studies involving tens of ion qubits, where fidelity has to be boosted to reduce error rates. By constructing decoherence-free subspaces[79] in ensembles of trapped ions, the present insensitivity to magnetic noise could be further enhanced, making the qubits better probes of, e.g., spin-spin interactions,[75] isotopic shifts,[80] violations of Lorentz invariance,[81,82] and searches for physics beyond the Standard Model.[1,7]

AUTHOR DECLARATIONS
Conflict of Interest

The authors have no conflicts to disclose.

Author Contributions

Elwin A. Dijck: Conceptualization (supporting); Formal analysis (lead); Investigation (lead); Methodology (lead); Supervision (supporting); Writing – original draft (lead); Writing – review & editing (lead). **Christian Warnecke**: Conceptualization (supporting); Formal analysis (supporting); Investigation (equal); Methodology (supporting); Supervision (supporting); Writing – original draft (supporting); Writing – review & editing (equal). **Malte Wehrheim**: Formal analysis (supporting); Investigation (equal); Methodology (supporting); Writing – review & editing (equal). **Ruben B. Henninger**: Formal analysis (supporting); Investigation (equal); Methodology (supporting); Writing – review & editing (supporting). **Julia Eff**: Investigation (supporting); Writing – review & editing (supporting). **Kostas Georgiou**: Investigation (supporting); Writing – review & editing (supporting). **Andrea Graf**: Resources (lead). **Stepan Kokh**: Investigation (equal); Writing – review & editing (supporting). **Lakshmi P. Kozhiparambil Sajith**: Investigation (supporting); Writing – review & editing (supporting). **Christopher Mayo**: Investigation (supporting); Writing – review & editing (supporting). **Vera M. Schäfer**: Investigation (supporting); Writing – review & editing (equal). **Claudia Volk**: Investigation (supporting); Writing –

review & editing (supporting). **Piet O. Schmidt**: Conceptualization (supporting); Funding acquisition (supporting); Writing – review & editing (equal). **Thomas Pfeifer**: Conceptualization (supporting); Funding acquisition (equal); Project administration (equal); Supervision (equal); Writing – review & editing (equal). **José R. Crespo López-Urrutia**: Conceptualization (lead); Funding acquisition (lead); Project administration (lead); Supervision (lead); Writing – original draft (supporting); Writing – review & editing (equal).

DATA AVAILABILITY

The data that support the findings of this study are available from the corresponding author upon reasonable request.

REFERENCES

[1] M. G. Kozlov, M. S. Safronova, J. R. Crespo López-Urrutia, and P. O. Schmidt, "Highly charged ions: Optical clocks and applications in fundamental physics," Rev. Mod. Phys. **90**, 045005 (2018).

[2] N.-H. Rehbehn, M. K. Rosner, H. Bekker, J. C. Berengut, P. O. Schmidt, S. A. King, P. Micke, M. F. Gu, R. Müller, A. Surzhykov, and J. R. Crespo López-Urrutia, "Sensitivity to new physics of isotope-shift studies using the coronal lines of highly charged calcium ions," Phys. Rev. A **103**, L040801 (2021).

[3] S.-Y. Liang, T.-X. Zhang, H. Guan, Q.-F. Lu, J. Xiao, S.-L. Chen, Y. Huang, Y.-H. Zhang, C.-B. Li, Y.-M. Zou, J.-G. Li, Z.-C. Yan, A. Derevianko, M.-S. Zhan, T.-Y. Shi, and K.-L. Gao, "Probing multiple electric-dipole-forbidden optical transitions in highly charged nickel ions," Phys. Rev. A **103**, 022804 (2021).

[4] J. C. Berengut, V. A. Dzuba, and V. V. Flambaum, "Enhanced laboratory sensitivity to variation of the fine-structure constant using highly charged ions," Phys. Rev. Lett. **105**, 120801 (2010).

[5] J. C. Berengut, V. A. Dzuba, V. V. Flambaum, and A. Ong, "Highly charged ions with E1, M1, and E2 transitions within laser range," Phys. Rev. A **86**, 022517 (2012).

[6] H. Bekker, A. Borschevsky, Z. Harman, C. H. Keitel, T. Pfeifer, P. O. Schmidt, J. R. Crespo López-Urrutia, and J. C. Berengut, "Detection of the $5p$–$4f$ orbital crossing and its optical clock transition in Pr^{9+}," Nat. Commun. **10**, 5651 (2019).

[7] S. G. Porsev, U. I. Safronova, M. S. Safronova, P. O. Schmidt, A. I. Bondarev, M. G. Kozlov, I. I. Tupitsyn, and C. Cheung, "Optical clocks based on the Cf^{15+} and Cf^{17+} ions," Phys. Rev. A **102**, 012802 (2020).

[8] I. Klaft, S. Borneis, T. Engel, B. Fricke, R. Grieser, G. Huber, T. Kühl, D. Marx, R. Neumann, S. Schröder, P. Seelig, and L. Völker, "Precision laser spectroscopy of the ground state hyperfine splitting of hydrogenlike $^{209}Bi^{82+}$," Phys. Rev. Lett. **73**, 2425–2427 (1994).

[9] V. M. Shabaev, M. Tomaselli, T. Kühl, A. N. Artemyev, and V. A. Yerokhin, "Ground-state hyperfine splitting of high-Z hydrogenlike ions," Phys. Rev. A **56**, 252–255 (1997).

[10] J. R. Crespo López-Urrutia, P. Beiersdorfer, K. Widmann, B. B. Birkett, A.-M. Mårtensson-Pendrill, and M. G. H. Gustavsson, "Nuclear magnetization distribution radii determined by hyperfine transitions in the $1s$ level of H-like ions $^{185}Re^{74+}$ and $^{187}Re^{74+}$," Phys. Rev. A **57**, 879–887 (1998).

[11] P. Beiersdorfer, S. B. Utter, K. L. Wong, J. R. Crespo López-Urrutia, J. A. Britten, H. Chen, C. L. Harris, R. S. Thoe, D. B. Thorn, E. Träbert, M. G. H. Gustavsson, C. Forssén, and A.-M. Mårtensson-Pendrill, "Hyperfine structure of hydrogenlike thallium isotopes," Phys. Rev. A **64**, 032506 (2001).

[12] S. Schiller, "Hydrogenlike highly charged ions for tests of the time independence of fundamental constants," Phys. Rev. Lett. **98**, 180801 (2007).

[13] N. S. Oreshkina, S. M. Cavaletto, N. Michel, Z. Harman, and C. H. Keitel, "Hyperfine splitting in simple ions for the search of the variation of fundamental constants," Phys. Rev. A **96**, 030501 (2017).

[14] L. V. Skripnikov, S. Schmidt, J. Ullmann, C. Geppert, F. Kraus, B. Kresse, W. Nörtershäuser, A. F. Privalov, B. Scheibe, V. M. Shabaev, M. Vogel, and A. V. Volotka, "New nuclear magnetic moment of ^{209}Bi: Resolving the bismuth hyperfine puzzle," Phys. Rev. Lett. **120**, 093001 (2018).

[15] W. Nörtershäuser, J. Ullmann, L. V. Skripnikov, Z. Andelkovic, C. Brandau, A. Dax, W. Geithner, C. Geppert, C. Gorges, M. Hammen, V. Hannen, S. Kaufmann, K. König, F. Kraus, B. Kresse, Y. A. Litvinov, M. Lochmann, B. Maaß, J. Meisner, T. Murböck, A. F. Privalov, R. Sánchez, B. Scheibe, M. Schmidt, S. Schmidt, V. M. Shabaev, M. Steck, T. Stöhlker, R. C. Thompson, C. Trageser, M. Vogel, A. Vollbrecht, A. V. Volotka, and C. Weinheimer, "The hyperfine puzzle of strong-field bound-state QED," Hyperfine Interact. **240**, 51 (2019).

[16] V. I. Yudin, A. V. Taichenachev, and A. Derevianko, "Magnetic-dipole transitions in highly charged ions as a basis of ultraprecise optical clocks," Phys. Rev. Lett. **113**, 233003 (2014).

[17] P. O. Schmidt, T. Rosenband, C. Langer, W. M. Itano, J. C. Bergquist, and D. J. Wineland, "Spectroscopy using quantum logic," Science **309**, 749–752 (2005).

[18] L. Schmöger, O. O. Versolato, M. Schwarz, M. Kohnen, A. Windberger, B. Piest, S. Feuchtenbeiner, J. Pedregosa, T. Leopold, P. Micke, A. K. Hansen, T. M. Baumann, M. Drewsen, J. Ullrich, P. O. Schmidt, and J. R. Crespo López-Urrutia, "Coulomb crystallization of highly charged ions," Science **347**, 1233–1236 (2015).

[19] L. Schmöger, M. Schwarz, T. M. Baumann, O. O. Versolato, B. Piest, T. Pfeifer, J. Ullrich, P. O. Schmidt, and J. R. Crespo López-Urrutia, "Deceleration, precooling, and multi-pass stopping of highly charged ions in Be^+ Coulomb crystals," Rev. Sci. Instrum. **86**, 103111 (2015).

[20] P. Micke, T. Leopold, S. A. King, E. Benkler, L. J. Spieß, L. Schmöger, M. Schwarz, J. R. Crespo López-Urrutia, and P. O. Schmidt, "Coherent laser spectroscopy of highly charged ions using quantum logic," Nature **578**, 60–65 (2020).

[21] S. A. King, L. J. Spieß, P. Micke, A. Wilzewski, T. Leopold, J. R. Crespo López-Urrutia, and P. O. Schmidt, "Algorithmic ground-state cooling of weakly coupled oscillators using quantum logic," Phys. Rev. X **11**, 041049 (2021).

[22] S. A. King, L. J. Spieß, P. Micke, A. Wilzewski, T. Leopold, E. Benkler, R. Lange, N. Huntemann, A. Surzhykov, V. A. Yerokhin, J. R. Crespo López-Urrutia, and P. O. Schmidt, "An optical atomic clock based on a highly charged ion," Nature **611**, 43–47 (2022).

[23] J. R. Crespo López-Urrutia, "Frequency metrology using highly charged ions," J. Phys.: Conf. Ser. **723**, 012052 (2016).

[24] R. J. Jones, K. D. Moll, M. J. Thorpe, and J. Ye, "Phase-coherent frequency combs in the vacuum ultraviolet via high-harmonic generation inside a femtosecond enhancement cavity," Phys. Rev. Lett. **94**, 193201 (2005).

[25] C. Gohle, T. Udem, M. Herrmann, J. Rauschenberger, R. Holzwarth, H. A. Schuessler, F. Krausz, and T. W. Hänsch, "A frequency comb in the extreme ultraviolet," Nature **436**, 234–237 (2005).

[26] I. Pupeza, C. Zhang, M. Högner, and J. Ye, "Extreme-ultraviolet frequency combs for precision metrology and attosecond science," Nat. Photonics **15**, 175–186 (2021).

[27] J. Nauta, J.-H. Oelmann, A. Borodin, A. Ackermann, P. Knauer, I. S. Muhammad, R. Pappenberger, T. Pfeifer, and J. R. Crespo López-Urrutia, "XUV frequency comb production with an astigmatism-compensated enhancement cavity," Opt. Express **29**, 2624–2636 (2021).

[28] C. Lyu, S. M. Cavaletto, C. H. Keitel, and Z. Harman, "Interrogating the temporal coherence of EUV frequency combs with highly charged ions," Phys. Rev. Lett. **125**, 093201 (2020).

[29] W. Paul, "Electromagnetic traps for charged and neutral particles," Rev. Mod. Phys. **62**, 531–540 (1990).

[30] H. Dehmelt, "Stored-ion spectroscopy," in *Advances in Laser Spectroscopy*, edited by F. T. Arecchi, F. Strumia, and H. Walther (Springer, Boston, MA, 1983), pp. 153–187.

[31] F. Diedrich and H. Walther, "Nonclassical radiation of a single stored ion," Phys. Rev. Lett. **58**, 203–206 (1987).

[32] J. I. Cirac and P. Zoller, "Quantum computations with cold trapped ions," Phys. Rev. Lett. **74**, 4091–4094 (1995).

[33] C. Monroe, D. M. Meekhof, B. E. King, W. M. Itano, and D. J. Wineland, "Demonstration of a fundamental quantum logic gate," Phys. Rev. Lett. **75**, 4714–4717 (1995).

[34] I. Georgescu, "Trapped ion quantum computing turns 25," Nat. Rev. Phys. **2**, 278 (2020).

[35] A. D. Ludlow, M. M. Boyd, J. Ye, E. Peik, and P. O. Schmidt, "Optical atomic clocks," Rev. Mod. Phys. **87**, 637–701 (2015).

[36]J. Stark, C. Warnecke, S. Bogen, S. Chen, E. A. Dijck, S. Kühn, M. K. Rosner, A. Graf, J. Nauta, J.-H. Oelmann, L. Schmöger, M. Schwarz, D. Liebert, L. J. Spieß, S. A. King, T. Leopold, P. Micke, P. O. Schmidt, T. Pfeifer, and J. R. Crespo López-Urrutia, "An ultralow-noise superconducting radio-frequency ion trap for frequency metrology with highly charged ions," Rev. Sci. Instrum. **92**, 083203 (2021).

[37]P. Micke, S. Kühn, L. Buchauer, J. R. Harries, T. M. Bücking, K. Blaum, A. Cieluch, A. Egl, D. Hollain, S. Kraemer, T. Pfeifer, P. O. Schmidt, R. X. Schüssler, C. Schweiger, T. Stöhlker, S. Sturm, R. N. Wolf, S. Bernitt, and J. R. Crespo López-Urrutia, "The Heidelberg compact electron beam ion traps," Rev. Sci. Instrum. **89**, 063109 (2018).

[38]P. Mandal, G. Sikler, and M. Mukherjee, "Simulation study and analysis of a compact einzel lens-deflector for low energy ion beam," J. Instrum. **6**, P02004 (2011).

[39]M. Brownnutt, M. Kumph, P. Rabl, and R. Blatt, "Ion-trap measurements of electric-field noise near surfaces," Rev. Mod. Phys. **87**, 1419–1482 (2015).

[40]P. Paasche, C. Angelescu, S. Ananthamurthy, D. Biswas, T. Valenzuela, and G. Werth, "Instabilities of an electron cloud in a Penning trap," Eur. Phys. J. D **22**, 183–188 (2003).

[41]W. Alt, "An objective lens for efficient fluorescence detection of single atoms," Optik **113**, 142–144 (2002).

[42]R. Noek, G. Vrijsen, D. Gaultney, E. Mount, T. Kim, P. Maunz, and J. Kim, "High speed, high fidelity detection of an atomic hyperfine qubit," Opt. Lett. **38**, 4735 (2013).

[43]K. Pyka, N. Herschbach, J. Keller, and T. E. Mehlstäubler, "A high-precision segmented Paul trap with minimized micromotion for an optical multiple-ion clock," Appl. Phys. B **114**, 231–241 (2013).

[44]J. D. Wong-Campos, K. G. Johnson, B. Neyenhuis, J. Mizrahi, and C. Monroe, "High-resolution adaptive imaging of a single atom," Nat. Photonics **10**, 606–610 (2016).

[45]S. Li, G. Li, W. Wu, Q. Fan, Y. Tian, P. Yang, P. Zhang, and T. Zhang, "High-numerical-aperture and long-working-distance objective for single-atom experiments," Rev. Sci. Instrum. **91**, 043104 (2020).

[46]T. Nordmann, S. Wickenhagen, M. Doležal, and T. E. Mehlstäubler, "Bichromatic UV detection system for atomically-resolved imaging of ions," Rev. Sci. Instrum. **94**, 063305 (2023).

[47]T. Leopold, S. A. King, P. Micke, A. Bautista-Salvador, J. C. Heip, C. Ospelkaus, J. R. Crespo López-Urrutia, and P. O. Schmidt, "A cryogenic radio-frequency ion trap for quantum logic spectroscopy of highly charged ions," Rev. Sci. Instrum. **90**, 073201 (2019).

[48]T. Dubielzig, S. Halama, H. Hahn, G. Zarantonello, M. Niemann, A. Bautista-Salvador, and C. Ospelkaus, "Ultra-low-vibration closed-cycle cryogenic surface-electrode ion trap apparatus," Rev. Sci. Instrum. **92**, 043201 (2021).

[49]J.-M. Asfour, F. Weidner, C. Bodendorf, A. Bode, A. G. Poleshchuk, R. K. Nasyrov, F. Grupp, and R. Bender, "Diffractive optics for precision alignment of Euclid space telescope optics (conference presentation)," in *Astronomical Optics: Design, Manufacture, and Test of Space and Ground Systems*, edited by P. Hallibert, T. B. Hull, and D. W. Kim (SPIE, 2017).

[50]T. F. Gloger, P. Kaufmann, D. Kaufmann, M. T. Baig, T. Collath, M. Johanning, and C. Wunderlich, "Ion-trajectory analysis for micromotion minimization and the measurement of small forces," Phys. Rev. A **92**, 043421 (2015).

[51]D. J. Berkeland, J. D. Miller, J. C. Bergquist, W. M. Itano, and D. J. Wineland, "Minimization of ion micromotion in a Paul trap," J. Appl. Phys. **83**, 5025–5033 (1998).

[52]J. Keller, H. L. Partner, T. Burgermeister, and T. E. Mehlstäubler, "Precise determination of micromotion for trapped-ion optical clocks," J. Appl. Phys. **118**, 104501 (2015).

[53]R. C. Thompson, "Ion Coulomb crystals," Contemp. Phys. **56**, 63–79 (2015).

[54]S. Knünz, M. Herrmann, V. Batteiger, G. Saathoff, T. W. Hänsch, and Th. Udem, "Sub-millikelvin spatial thermometry of a single Doppler-cooled ion in a Paul trap," Phys. Rev. A **85**, 023427 (2012).

[55]V. Rajagopal, J. P. Marler, M. G. Kokish, and B. C. Odom, "Trapped ion chain thermometry and mass spectrometry through imaging," Eur. J. Mass Spectrom. **22**, 1 (2016).

[56]R. Blatt, P. Zoller, G. Holzmüller, and I. Siemers, "Brownian motion of a parametric oscillator: A model for ion confinement in radio frequency traps," Z. Phys. D: At., Mol. Clusters **4**, 121–126 (1986).

[57]W. Meissner and R. Ochsenfeld, "Ein neuer effekt bei eintritt der supraleitfähigkeit," Naturwissenschaften **21**, 787–788 (1933).

[58]C. Vallet, M. Boloré, B. Bonin, J. P. Charrier, B. Daillant, J. Gratadour, F. Koechlin, and H. Safa, "Flux trapping in superconducting cavities," in H. Heino, H. Homeyer, and C. Petit-Jean-Genaz (Eds.) *Proc. EPAC'92* (Éditions Frontières, 1992), pp. 1295–1297.

[59]H. Padamsee, "The science and technology of superconducting cavities for accelerators," Supercond. Sci. Technol. **14**, R28 (2001).

[60]Y. B. Kim, C. F. Hempstead, and A. R. Strnad, "Flux-flow resistance in type-II superconductors," Phys. Rev. **139**, A1163–A1172 (1965).

[61]B. Bonin and R. W. Röth, "Q degradation of niobium cavities due to hydrogen contamination," Part. Accel. **40**, 59–83 (1992).

[62]J. P. Gaebler, T. R. Tan, Y. Lin, Y. Wan, R. Bowler, A. C. Keith, S. Glancy, K. Coakley, E. Knill, D. Leibfried, and D. J. Wineland, "High-fidelity universal gate set for ^{9}Be$^+$ ion qubits," Phys. Rev. Lett. **117**, 060505 (2016).

[63]N. F. Ramsey, "A molecular beam resonance method with separated oscillating fields," Phys. Rev. **78**, 695–699 (1950).

[64]NIST Ion Storage Group, ARTIQ (Advanced Real-Time Infrastructure for Quantum Physics), 2017.

[65]D. S. Chuchelov, E. A. Tsygankov, S. A. Zibrov, M. I. Vaskovskaya, V. V. Vassiliev, A. S. Zibrov, V. I. Yudin, A. V. Taichenachev, and V. L. Velichansky, "Central Ramsey fringe identification by means of an auxiliary optical field," J. Appl. Phys. **126**, 054503 (2019).

[66]N. Shiga, W. M. Itano, and J. J. Bollinger, "Diamagnetic correction to the ^{9}Be$^+$ ground-state hyperfine constant," Phys. Rev. A **84**, 012510 (2011).

[67]T. Ruster, C. T. Schmiegelow, H. Kaufmann, C. Warschburger, F. Schmidt-Kaler, and U. G. Poschinger, "A long-lived Zeeman trapped-ion qubit," Appl. Phys. B **122**, 254 (2016).

[68]I. Altarev, E. Babcock, D. Beck, M. Burghoff, S. Chesnevskaya, T. Chupp, S. Degenkolb, I. Fan, P. Fierlinger, A. Frei, E. Gutsmiedl, S. Knappe-Grüneberg, F. Kuchler, T. Lauer, P. Link, T. Lins, M. Marino, J. McAndrew, B. Niessen, S. Paul, G. Petzoldt, U. Schläpfer, A. Schnabel, S. Sharma, J. Singh, R. Stoepler, S. Stuiber, M. Sturm, B. Taubenheim, L. Trahms, J. Voigt, and T. Zechlau, "A magnetically shielded room with ultra low residual field and gradient," Rev. Sci. Instrum. **85**, 075106 (2014).

[69]T. D. Ladd, F. Jelezko, R. Laflamme, Y. Nakamura, C. Monroe, and J. L. O'Brien, "Quantum computers," Nature **464**, 45–53 (2010).

[70]T. Monz, P. Schindler, J. T. Barreiro, M. Chwalla, D. Nigg, W. A. Coish, M. Harlander, W. Hänsel, M. Hennrich, and R. Blatt, "14-qubit entanglement: Creation and coherence," Phys. Rev. Lett. **106**, 130506 (2011).

[71]L. M. K. Vandersypen and I. L. Chuang, "NMR techniques for quantum control and computation," Rev. Mod. Phys. **76**, 1037–1069 (2005).

[72]D. Leibfried, R. Blatt, C. Monroe, and D. Wineland, "Quantum dynamics of single trapped ions," Rev. Mod. Phys. **75**, 281–324 (2003).

[73]S. Kotler, N. Akerman, Y. Glickman, A. Keselman, and R. Ozeri, "Single-ion quantum lock-in amplifier," Nature **473**, 61–65 (2011).

[74]T. P. Harty, D. T. C. Allcock, C. J. Ballance, L. Guidoni, H. A. Janacek, N. M. Linke, D. N. Stacey, and D. M. Lucas, "High-fidelity preparation, gates, memory, and readout of a trapped-ion quantum bit," Phys. Rev. Lett. **113**, 220501 (2014).

[75]S. Kotler, N. Akerman, N. Navon, Y. Glickman, and R. Ozeri, "Measurement of the magnetic interaction between two bound electrons of two separate ions," Nature **510**, 376–380 (2014).

[76]P. Wang, C.-Y. Luan, M. Qiao, M. Um, J. Zhang, Y. Wang, X. Yuan, M. Gu, J. Zhang, and K. Kim, "Single ion qubit with estimated coherence time exceeding one hour," Nat. Commun. **12**, 233 (2021).

[77]H. Häffner, C. F. Roos, and R. Blatt, "Quantum computing with trapped ions," Phys. Rep. **469**, 155–203 (2008).

[78]R. Blatt and C. F. Roos, "Quantum simulations with trapped ions," Nat. Phys. **8**, 277–284 (2012).

[79]D. A. Lidar, I. L. Chuang, and K. B. Whaley, "Decoherence-free subspaces for quantum computation," Phys. Rev. Lett. **81**, 2594–2597 (1998).

[80]T. Manovitz, R. Shaniv, Y. Shapira, R. Ozeri, and N. Akerman, "Precision measurement of atomic isotope shifts using a two-isotope entangled state," Phys. Rev. Lett. **123**, 203001 (2019).

[81]T. Pruttivarasin, M. Ramm, S. G. Porsev, I. I. Tupitsyn, M. S. Safronova, M. A. Hohensee, and H. Häffner, "Michelson–Morley analogue for electrons using trapped ions to test Lorentz symmetry," Nature **517**, 592–595 (2015).

[82]L. S. Dreissen, C.-H. Yeh, H. A. Fürst, K. C. Grensemann, and T. E. Mehlstäubler, "Improved bounds on Lorentz violation from composite pulse Ramsey spectroscopy in a trapped ion," Nat. Commun. **13**, 7314 (2022).

16 October 2023 09:48:25